2016

Modeling of Initially Subcooled Flashing Vortex Flow in the Nozzle for Possible Applications in the Control of Ejector Cooling Cycles

Jingwei Zhu
ACRC, University of Illinois at Urbana-Champaign, jzhu50@illinois.edu

Stefan Elbel
elbel@illinois.edu

Modeling of Initially Subcooled Flashing Vortex Flow in the Nozzle for Possible Applications in the Control of Ejector Cooling Cycles

Jingwei ZHU, Stefan ELBEL*

Department of Mechanical Science and Engineering,
University of Illinois at Urbana-Champaign,
1206 West Green Street, Urbana, IL, 61801, USA
Phone: (217) 244-1531, Fax: (217) 333-1942, Email: elbel@illinois.edu

* Corresponding Author

ABSTRACT

Ejectors are known to be beneficial to vapor compression cycle performance as they can recover the kinetic energy released during the expansion instead of dissipating it in a throttling process. It is desirable to introduce an adjustable feature to the ejector so that ejector cycle performance can be optimized under different working conditions, which could make ejector technology more suitable for real world applications. Vortex control is a nozzle control mechanism which can possibly be applied to the control of ejector cooling cycles. It utilizes an adjustable vortex at the nozzle inlet to control the nozzle restrictiveness without having to change physical dimensions of the nozzle geometry. In this paper, two different approaches are employed to model the initially subcooled flashing vortex flow in a convergent nozzle at steady state. The first approach assumes that bubble nucleation during the depressurization in the nozzle all occurs at the nozzle wall. Bubbles are regarded as spherical particles that grow and move in the liquid flow field. The second approach assumes that there is an evaporation wave at the nozzle throat. The bubble generation in the upstream of the evaporation wave is neglected, thus the fluid in the upstream of the evaporation wave is assumed to be single-phase incompressible liquid. The modeling results are presented and compared with the experimental results. It has been concluded that bubble nucleation may not all occur at the nozzle wall at high degree of metastability. Nucleation in the bulk of the liquid might be dominant and should possibly be taken into consideration in the modeling. Pressure reduction is required for the kinetic energy increase of the nozzle flow in the azimuthal direction when there is inlet vortex introduced. For the same mass flow rate through the nozzle, the pressure difference from the nozzle inlet to the center of the nozzle throat increases as the inlet vortex becomes stronger. Therefore, less mass flow rate can be driven through the nozzle with stronger inlet vortex for the same degree of metastability at the throat and the same inlet conditions. The change in total mass flow rate is smaller with larger surface roughness for the same inlet vortex strength.

1. INTRODUCTION

Ejectors which can recover the kinetic energy released during the expansion process are known to be beneficial to vapor compression cycle performance (Elbel and Hrnjak, 2008; Lawrence and Elbel, 2014). However, ejector cycle performance is usually sensitive to working condition changes which are common in real world applications. Different working conditions require different ejector geometries to achieve maximum performance. Slightly different geometries may result in substantially different COPs under the same conditions. Therefore, it is desirable to introduce an adjustable feature to the ejector so that ejector cycle performance can be optimized under different working conditions, which could make ejector technology more suitable for real world applications (Sumeru *et al*., 2012).

The ejector motive nozzle restrictiveness is one of the key factors that affect ejector cycle COP. It has a direct impact on motive mass flow rate. Zhu and Elbel (2016) were the first to introduce vortex control to ejector for the control of ejector cooling cycles. A vortex ejector which employs the vortex control to adjust motive nozzle restrictiveness differs from a conventional ejector in that an adjustable vortex is generated at the ejector motive inlet,

as is shown in Figure 1. The motive inlet vortex can be created by injecting part of the motive flow tangentially. After injection the tangential flow will be mixed with the axial motive flow. The total mass flow rate passing through the vortex nozzle is equal to the sum of mass flow rates entering through the nozzle's axial and tangential flow inlets. The ejector cooling cycle using a vortex ejector is almost the same as the conventional ejector cooling cycle. The only difference is that the flow at the condenser outlet of the vortex ejector cooling cycle is separated into two streams. One stream enters the vortex ejector through the motive flow tangential inlet and another enters through the motive flow axial inlet. In such a way, a vortex is created at the ejector motive inlet. The ratio of mass flow rates through the two inlets can be adjusted by a valve installed at the motive flow tangential inlet, thereby changing the vortex strength. The pressure drop across the control valve is usually small. It can be assumed that the thermodynamic state at the motive nozzle inlet after the vortex is introduced (downstream of the tangential inlet valve) is the same as the refrigerant state at the condenser outlet.

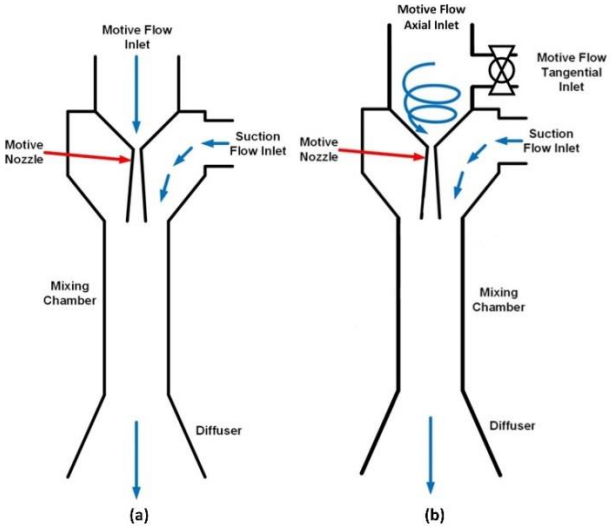

Figure 1: (a) Conventional ejector and (b) vortex ejector

Zhu and Elbel's tests on vortex nozzle with initially subcooled R134a show that the strength of the nozzle inlet vortex can change the restrictiveness of the two-phase nozzle without the need of changing the nozzle geometry. The nozzle becomes more restrictive as the strength of the vortex increases. The mass flow rate can be reduced by 36% with vortex control under the same inlet and outlet conditions. The control range of inlet pressures and mass flow rates that can be achieved by vortex control appears to be large enough to be applicable for real world applications.

In the following sections, two approaches with different assumptions to model the initially subcooled flashing vortex flow in a convergent nozzle at steady state will be presented. The modeling results will be provided and compared with the experimental results by Zhu and Elbel (2016).

2. FLASHING FLOW IN NOZZLES

In nozzles, the liquid pressure may be dropped far below the saturation pressure without immediate occurrence of boiling due to the limited rate of phase change. The limitation on phase change rate during the initial departure from saturation pressure is mainly due to the absence of interfacial area and the lack of thermal driving potential. As a result, the liquid becomes superheated or metastable. The bubble nucleation within the nozzle starts either at cavity defects on the nozzle wall or at the imbedded impurities in the bulk of the liquid. In small geometries which have large surface-to-volume ratio, nucleation will occur generally at cavity defects on the nozzle wall. As the geometry increases in size so that the surface-to-volume ratio decreases, it is expected that bulk nucleation will become important. It is not clear when the transition from wall-dominated to bulk-dominated nucleation will take place (Blinkov *et al.*, 1993). Wave-like evaporation has been reported by many researchers in metastable liquid evaporation at high degree of metastability and in short nozzles. The phase change process is confined to a narrow and observable region with undisturbed metastable liquid in the upstream and a two-phase mixture in the downstream (Simoes-Moreira and Shepherd, 1999). It was shown in the experiments examined with subcooled inlet by Abuaf *et al*. (1983) that flashing inception invariably occurred very close to the nozzle throat regardless of the

degree of inlet subcooling. A sudden evaporation at the nozzle throat was also observed in Zhu and Elbel's (2016) visualization of initially subcooled flashing vortex flow in the nozzle when the nozzle outlet pressure is low. Thermodynamic equilibrium in the bulk of the fluid was attained almost instantly across the evaporation wave (Edwards and O'Brien, 1970).

In this paper, two different approaches are employed to model the initially subcooled flashing vortex flow in a convergent nozzle at steady state. The first approach assumes that bubble nucleation during the depressurization in the nozzle all occurs at the nozzle wall. Bubbles are regarded as spherical particles that grow and move in the liquid flow field. The bubble growth after departure from the nozzle wall is heat transfer controlled. The second approach assumes that there is an evaporation wave at the nozzle throat. The bubble generation in the upstream of the evaporation wave is neglected, thus the fluid in the upstream of the evaporation wave is assumed to be single-phase incompressible liquid. When the flow is choked, it is assumed that the degree of metastability, which was defined by Simoes-Moreira and Bullard (2003) as

$$\Pi = \frac{p_{sat} - p_{meta}}{p_{sat}} \tag{1}$$

where p_{meta} is the metastable pressure, in the upstream of the evaporation wave does not vary with vortex strength and depressurization rate and keeps constant for the same nozzle inlet pressure and subcooling.

3. GOVERNING EQUATIONS

The continuity equation for each phase is

$$\frac{\partial \rho_k}{\partial t} + \nabla \cdot (\rho_k \boldsymbol{v}_k) = 0 \tag{2}$$

The liquid density is assumed to be constant, which equals the inlet subcooled liquid density. The vapor density is assumed to be the density of saturated vapor at local liquid pressure.

The momentum equation for each phase is

$$\frac{\partial \rho_k \boldsymbol{v}_k}{\partial t} + \nabla \cdot (\rho_k \boldsymbol{v}_k \boldsymbol{v}_k) = -\nabla p_k + \nabla \cdot \boldsymbol{\varepsilon}_k \tag{3}$$

where $\boldsymbol{\varepsilon}_k$ is the viscous stress.

The balance of energy can be written as

$$\frac{\partial \rho_k (u_k + \frac{v_k^2}{2})}{\partial t} + \nabla \cdot \left[\rho_k \left(u_k + \frac{v_k^2}{2}\right) \boldsymbol{v}_k\right] = -\nabla \cdot \boldsymbol{q}_k + \nabla \cdot (\boldsymbol{\sigma}_k \cdot \boldsymbol{v}_k) \tag{4}$$

where $\boldsymbol{q}_k$ and $\boldsymbol{\sigma}_k$ represent the heat flux and the surface stress tensor, respectively.

The interfacial mass balance between the liquid and vapor phases is

$$\sum_{k=1}^{2} \dot{m}_k = 0 \tag{5}$$

where $\dot{m}_k \equiv \rho_k \boldsymbol{n}_k \cdot (\boldsymbol{v}_k - \boldsymbol{v}_i)$ is the interfacial mass efflux from the kth-phase.

A spherical coordinate system, as shown in Figure 2, is used for simplicity of analysis. Since the flow is assumed to be at steady state and axisymmetric, $\frac{\partial}{\partial t} = 0$, $\frac{\partial}{\partial \phi} = 0$.

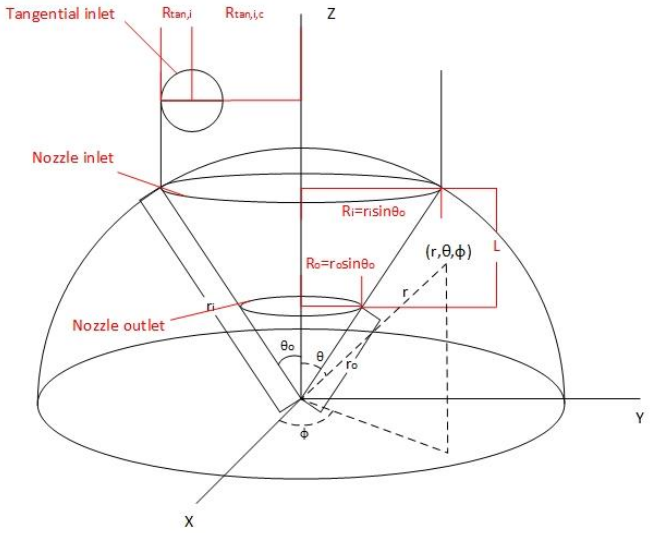

Figure 2: Schematic of a convergent nozzle in a spherical coordinate system and a Cartesian coordinate system

3.1 Bubble Departure (In Approach 1 Considering Only Nozzle Wall Nucleation)

Bubble nucleation and departure are assumed to take place at where the liquid superheat is larger than zero. The departure radius of a bubble is given by (Shin and Jones, 1993)

$$R_{depart} = \sqrt{\frac{\mu_{liquid}}{\tau_{wall}}\sqrt{\frac{4\sigma R_c}{C_D\rho_{liquid}}}} \tag{6}$$

where the drag coefficient C_D is assumed to be 0.5, R_c is the minimum cavity size and is approximated as

$$R_c \approx \frac{2\sigma T_{sat}}{\rho_{vapor}h_{fg}(T_{liquid}-T_{sat})} \tag{7}$$

The frequency of bubble departure per unit area is assumed to be $C_{depart}\left(T_{liquid} - T_{sat}\right)^3$(Shin and Jones, 1993), where C_{depart} is a constant.

3.2 Single Bubble Motion (In Approach 1 Considering Only Nozzle Wall Nucleation)

It is assumed that vapor generated during the expansion in the nozzle is in the form of spherical bubbles. After the departure from the nozzle wall, each bubble is assumed to be moving in an infinite medium. The motion and growth of bubbles can affect the liquid flow field. Therefore, the bubbles and the liquid are two-way coupled. When a bubble is about to depart from the wall, its velocity is assumed to be zero.

The resultant force on a single bubble can be expressed as

$$\boldsymbol{F}_{resultant} = \boldsymbol{F}_{pressure,r} + \boldsymbol{F}_{pressure,\theta} + \boldsymbol{F}_{drag} \tag{8}$$

$$\boldsymbol{F}_{pressure,r} = -\int_{V_{bubble}}\frac{\partial p}{\partial r}dV\boldsymbol{e}_r \approx -\frac{\partial p}{\partial r}V_{bubble}\boldsymbol{e}_r \tag{9}$$

$$\boldsymbol{F}_{pressure,\theta} = -\int_{V_{bubble}}\frac{\partial p}{r\partial\theta}dV\boldsymbol{e}_\theta \approx -\frac{\partial p}{r\partial\theta}V_{bubble}\boldsymbol{e}_\theta \tag{10}$$

The generalized drag force on a bubble is modeled as

$$\boldsymbol{F}_{drag} = \boldsymbol{F}^D_{drag} + \boldsymbol{F}^V_{drag} \tag{11}$$

where $\boldsymbol{F}^D_{drag}$ and $\boldsymbol{F}^V_{drag}$are the standard drag force and the virtual mass force, respectively.

The standard drag force can be written as

$$\boldsymbol{F}^D_{drag} = -\frac{C_D\rho_{liquid}\boldsymbol{v}_{relative}|\boldsymbol{v}_{relative}|\pi R^2_{bubble}}{2} \tag{12}$$

where the relative velocity of the bubble with respect to the surrounding liquid is $\boldsymbol{v}_{relative} = \boldsymbol{v}_{bubble} - \boldsymbol{v}_{liquid}$. The drag coefficient is given by an empirical correlation as

$$C_D = \frac{24}{Re}(1 + 0.1\,Re^{0.75}) \tag{13}$$

where the Reynolds number $Re = \rho_{liquid}|v_{relative}|\frac{2R_{bubble}}{\mu_{liquid}}$.

The virtual mass force can be written as

$$\boldsymbol{F}^V_{drag} = \frac{\rho_{liquid}V_{bubble}}{2}\left(\frac{d\boldsymbol{v}_{liquid}}{dt} - \frac{d\boldsymbol{v}_{bubble}}{dt}\right) \tag{14}$$

3.3 Bubble Growth (In Approach 1 Considering Only Nozzle Wall Nucleation)

The bubble mass growth after the departure from the nozzle wall is assumed to be heat transfer controlled and is approximated by quasi steady state. It is assumed that at each moment of time the heat transfer coefficient is given by expressions valid for the corresponding constant radius moving bubble. For potential flow around a constant size bubble the average Nusselt number is given by

$$\overline{Nu}_{sphere} = \frac{\bar{h}D_{bubble}}{K} = 2 + \left[0.4Re^{\frac{1}{2}} + 0.06Re^{\frac{2}{3}}\right]Pr^{0.4}\left(\frac{\mu_{liquid,\infty}}{\mu_{liquid,s}}\right)^{\frac{1}{4}} \tag{15}$$

where $\mu_{liquid,s}$ is the liquid dynamic viscosity evaluated at the bubble surface temperature. The Reynolds number is evaluated based on the relative velocity of bubble with respect to the liquid and $\mu_{liquid,\infty}$.

This correlation is valid for 3.5<Re<80000 and 0.7<Pr<380 (Whitaker, 1972).

The mass growth of each bubble is obtained from an energy balance on the bubble:

$$\frac{d(m_{bubble})}{dt}h_{fg} = 4\pi R^2_{bubble}\bar{h}(T_{liquid,\infty} - T_{sat}) \tag{16}$$

3.4 Boundary Conditions

The flow at the nozzle inlet is subcooled liquid. There is no bubble mass flow rate entering the nozzle through the inlet.

$$v_r(r_i,\theta) = -\frac{\dot{m}_{total}}{2\pi r_i^2 \rho_{liquid}(1-\cos\theta_o)} \quad (17)$$

$$v_\theta(r,\theta_o) = 0 \quad (18)$$

$$v_\phi(r_i,\theta) = v_\phi(r_i,\theta_o)\frac{\sin\theta}{\sin\theta_o} \quad (19)$$

$$p(r_i,\theta_o) = p_i \quad (20)$$

$$p(r_o,0) = p_o \quad (21)$$

$$T(r_i,\theta) = T_i \quad (22)$$

where $\dot{m}_{total}$ is the total mass flow rate through the nozzle, θ_o is the half-angle of nozzle convergent part, p_i and p_o are the nozzle inlet and outlet pressures, respectively, T_i is the inlet temperature. p_o is assumed to be the lowest pressure at the outlet surface $r = r_o$. The temperature change in adiabatic liquid flow during the expansion in the nozzle is generally negligible. The liquid temperature in the nozzle is assumed to be constant and equal to T_i.

It is assumed that angular momentum flux is unchanged from where the tangential inlet flow mixes with the axial inlet flow to the nozzle inlet.

$$\dot{m}_{tan,i}\bar{v}_{tan,i}R_{tan,i,c} = \frac{\dot{m}_{total}r_i}{1-\cos\theta_o}\frac{v_\phi(r_i,\theta_o)}{\sin\theta_o}\left(\frac{\cos^3\theta_o}{3} - \cos\theta_o + \frac{2}{3}\right) \quad (23)$$

where $\bar{v}_{tan,i} = \dot{m}_{tan,i}/\rho_{liquid}\pi R_{tan,i}^2$ and $\dot{m}_{tan,i}$ is the tangential inlet mass flow rate. $R_{tan,i,c}$ and $R_{tan,i}$ are as shown in Figure 2. $v_\phi(r_i,\theta_o)$ can be calculated once $\dot{m}_{tan,i}$, $\dot{m}_{total}$ and the convergent nozzle dimensions are known.

4. SOLUTION PROCEDURE

4.1 Mesh Configuration of the Computational Domain

In order to discretize the governing equations, uniform mesh is generated for the computational domain. For the approach considering only nozzle wall nucleation, bubble departure is assumed to occur at where the liquid superheat is larger than or equal to zero. Uniform computational meshes of 400 nodes and 200 nodes are created for the no-bubble zone and the bubble departure zone, respectively. Under the conditions considered in the simulation, the location where bubble departure starts is very close to the nozzle throat. The distance between the bubble departure inception point and the nozzle throat is less than one-tenth of the total length of the nozzle. For the second approach assuming evaporation wave at the throat, a uniform computational meshes of 400 nodes is used.

4.2 Liquid Flow Field Assumption

It is assumed that the vapor mass flow rate in the nozzle compared with that of liquid is negligible. Therefore, $\dot{m}_{total} \approx \dot{m}_{liquid}$.

The liquid velocity field in the whole computational domain of the convergent nozzle is assumed to be

$$v_r(r,\theta) = v_r(r) \quad (24)$$

$$v_\theta(r,\theta) = 0 \quad (25)$$

$$v_\phi(r,\theta) = v_\phi(r,\theta_o)\frac{\sin\theta}{\sin\theta_o} \quad (26)$$

When there is no bubble existing in the flow and with the above velocity profile assumptions, the momentum equation in the θ direction can be written as

$$-\frac{v_\phi^2(r,\theta)\cot\theta}{r} = -\frac{1}{\rho_{liquid}r}\frac{\partial p}{\partial\theta} \quad (27)$$

After integration

$$p(r,\theta) = p(r,\theta_o) - \frac{\rho_{liquid}v_\phi^2(r,\theta_o)}{\sin^2\theta_o}\frac{\sin^2\theta_o - \sin^2\theta}{2} \quad (28)$$

4.3 Wall Shear Stress Modeling

The wall shear stress is modeled as:

$$\tau_{wall}(r) = \frac{1}{8}\lambda\rho_{liquid}[v_r^2(r,\theta_o) + v_\phi^2(r,\theta_o)] \quad (29)$$

where λ is the Darcy–Weisbach friction factor which is modeled as a function of surface roughness ϵ and Reynolds number Re:

$$\frac{1}{\sqrt{\lambda}} = -2\log_{10}\left(\frac{\epsilon}{3.7D} + \frac{5.74}{Re^{0.9}}\right) \text{ (Swamee–Jain equation)} \quad (30)$$

$$Re = \rho_{liquid}\sqrt{v_r^2(r,\theta_o) + v_\phi^2(r,\theta_o)}D_N/\mu_{liquid} \quad (31)$$

where the nozzle diameter $D_N = 2R_N = 2rsin(\theta_o)$.

$$\tau_\phi(r) = -\frac{v_\phi(r,\theta_o)}{\sqrt{v_r^2(r,\theta_o)+v_\phi^2(r,\theta_o)}}\tau_{wall}(r) \quad (32)$$

$$\tau_r(r) = -\frac{v_r(r,\theta_o)}{\sqrt{v_r^2(r,\theta_o)+v_\phi^2(r,\theta_o)}}\tau_{wall}(r) \quad (33)$$

4.4 Numerical Method

The governing equations have been discretized based on the finite volume method. The bubble motion and growth is approximated by Euler method. The frequency of bubbles departure between $r[i]$ and $r[i+1]$ is calculated as

$$n[i] = C_{depart}\left(T_{liquid}[i] - T_{sat}[i]\right)^3 \pi(r[i] + r[i+1])sin(\theta_o)\,(r[i] - r[i+1]). \quad (34)$$

The contributions of vapor in the mass and momentum equations are regarded as negligible.

The momentum equations are discretized by using first order upwind differencing. The shear stress from the velocity gradient in the radial direction is not considered.

5. RESULTS AND DISCUSSION

5.1 Simulation and Experimental Test Conditions

A summary of geometric parameters of the vortex convergent-divergent nozzle used for experimental tests in Zhu and Elbel (2016) is provided in Table 1. The nozzle throat has been measured with higher accuracy as small change in throat diameter may result in large difference in flow rate.

Table 1: Vortex nozzle geometric parameters

Nozzle inlet diameter (mm)	15.0
Nozzle throat diameter (mm)	1.03
Nozzle outlet diameter (mm)	1.7
Nozzle convergent part length (mm)	9.9
Nozzle divergent part length (mm)	40.0
Tangential inlet inner diameter (mm)	2.0

In the simulation, only the convergent part of the nozzle is considered and it is assumed that the choked mass flow rate through the nozzle is determined by the convergent part of the nozzle. The geometric parameters in the simulation are kept the same as shown in Table 1.

5.2 Considering Only Nozzle Wall Nucleation

C_{depart} is set to 8.7E15 $m^{-2}s^{-1}K^{-3}$ so that the choked nozzle total mass flow rate with no inlet vortex matches the experimental results. The wall surface roughness is set to 0.1 mm. Figure 3 shows the influence of the vortex nozzle outlet pressure on the vortex nozzle total mass flow rate at different inlet vortex strengths under constant inlet conditions p_i = 925 kPa and T_i = 36 ℃. Vortex strength in this paper is defined as the ratio of the nozzle tangential inlet mass flow rate to the total mass flow rate

$$Vortex\ strength = \frac{\dot{m}_{tan}}{\dot{m}_{total}} \quad (35)$$

It can be observed that when there is no inlet vortex, the flow is choked at low nozzle outlet pressure as decrease in outlet pressure does not increase the mass flow rate significantly. However, after the inlet vortex is applied, the flow may no longer be choked even at low nozzle pressure. For example, when the vortex strength is 0.6, the total mass flow rate increases from 16.5 g s^{-1} to 16.9 g s^{-1} as the outlet pressure decreases from 385 kPa to 176 kPa. Because of the pressure gradient in the θ direction caused by the vortex, the pressure near the wall is much higher than the pressure at the nozzle centerline at the same radial distance from the spherical coordinate origin. The high pressure near the wall suppresses the bubble departure frequency which is proportional to $[T_{liquid} - T_{sat}(p_{wall})]^3$ and therefore there is not enough bubble generation to choke the flow. Nevertheless, it has been observed in the experiments that the nozzle flow can always be choked at low outlet pressure regardless of the inlet vortex strength, as is shown in Figure 4. Therefore, at high degree of metastability there might be nucleation sites other than those at the nozzle wall, which are very likely in the bulk of the liquid, that trigger enough bubble generation to choke the flow.

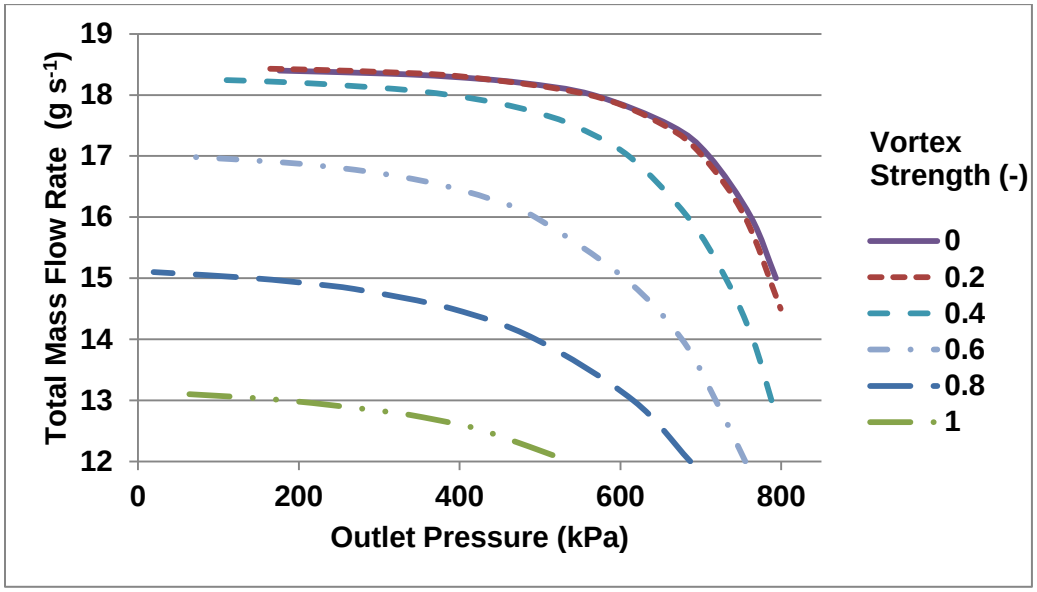

Figure 3: Influence of vortex nozzle outlet pressure on the vortex nozzle total mass flow rate at different vortex strengths under constant inlet conditions $p_i = 925$ kPa and $T_i = 36$ ℃ by modeling

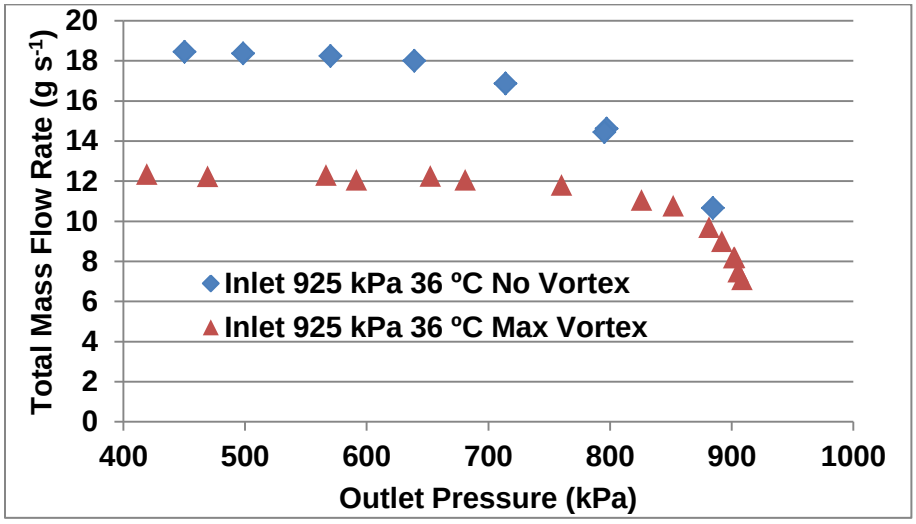

Figure 4: Influence of vortex nozzle (convergent-divergent) outlet pressure on the vortex nozzle total mass flow rate under constant inlet conditions $p_i = 925$ kPa and $T_i = 36$ ℃ by experiments (Zhu and Elbel, 2016)

Figure 5 compares the choked mass flow rates at different inlet vortex strength from the experiments with modeling results at low nozzle outlet pressures and constant inlet conditions p_i = 925 kPa and T_i = 36 ℃. It can be observed in the modeling results that the total mass flow rate decreases as the vortex becomes stronger. However, poor agreement has been achieved between the experimental and modeling results. The vortex strength at which the total mass flow rate starts to drop significantly is about 0.3 in the modeling results, while that achieved from the experiments is about 0.1.

The simulation results achieved by the first approach suggest that at high degree of metastability the bubble nucleation may not all occur at the nozzle wall. Nucleation in the bulk of the liquid might be dominant and should possibly be taken into consideration in the modeling.

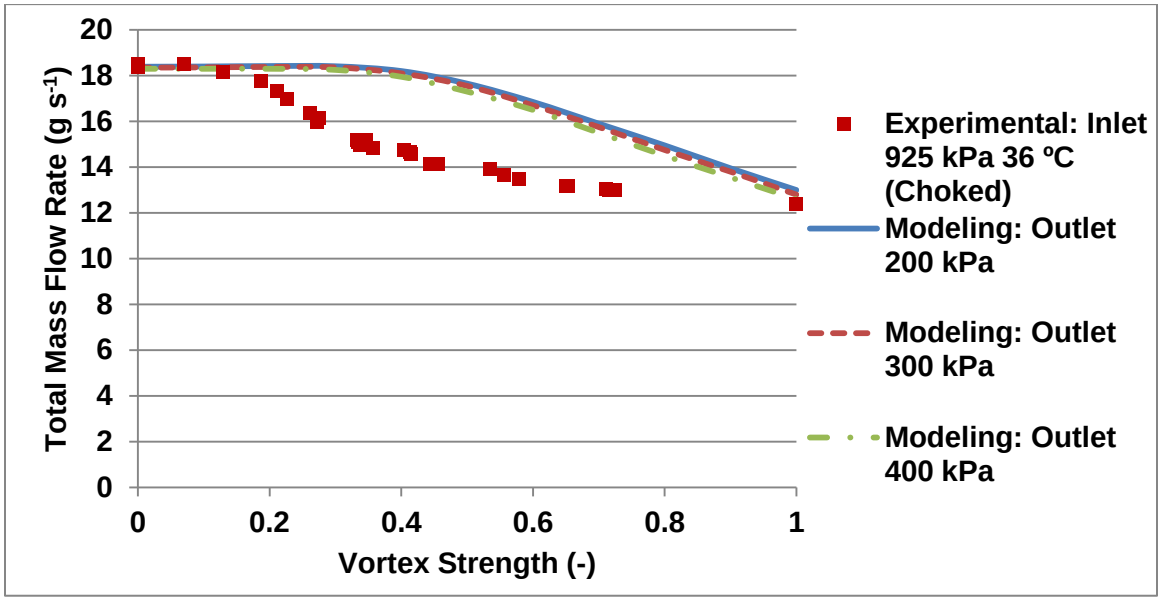

Figure 5: Comparison of choked mass flow rates at different inlet vortex strength from the experiments with modeling results by approach 1 at low nozzle outlet pressures and constant inlet conditions $p_i = 925$ kPa and $T_i = 36$ ℃

5.3 Evaporation Wave at the Nozzle Throat

For the second approach, only simulation results for the choked vortex nozzle flow are presented.

For inlet conditions p_i = 925 kPa and T_i = 36 ℃, the metastable pressure in the upstream of the evaporation wave when the flow is choked is assumed to be 753 kPa so that the choked nozzle total mass flow rate with no inlet vortex matches the experimental results. The lowest pressure at the convergent nozzle outlet surface $r = r_o$ is assumed to be equal to this metastable pressure when the flow is choked. The modeling results for choked flow with different nozzle wall surface roughnesses are compared with the experimental results in Figure 6. The results achieved by the second approach agree with the experimental results for choked flow (high degree of metastability) better than the first approach.

The influence of inlet vortex strength on the nozzle flow from the modeling shows similar trend as in the experimental results. When the vortex strength is close to zero, the total choked mass flow rate through the nozzle is almost unaffected as the vortex strength increases. When the vortex strength increases to around 0.1, significant drop in the total choked mass flow rate can be observed. The decreasing rate of the total choked mass flow rate will first increase and eventually slows down at large vortex strength.

The influence of inlet vortex on the nozzle flow rate can be explained as follows:

During the depressurization of the vortex flow in the convergent nozzle, both azimuthal and radial velocities increase from the nozzle inlet to the throat. To drive the same mass flow rate through the nozzle, kinetic energy increase in the radial direction is the same from the nozzle inlet to the outlet regardless of the vortex strength. However, additional pressure reduction is required for the kinetic energy increase in the azimuthal direction when there is inlet vortex introduced. The stronger the inlet vortex is, the more kinetic energy increase in the azimuthal direction is and the more pressure reduction is needed. Therefore, for the same mass flow rate through the nozzle, the pressure difference from the nozzle inlet to the center of the nozzle throat (i.e. the lowest pressure point at the throat) increases as the inlet vortex becomes stronger. Since the metastable pressure at the throat when the flow is choked is assumed to be constant for the same nozzle inlet pressure and temperature, less mass flow rate can be driven through the nozzle with stronger inlet vortex.

The larger the surface roughness is, the larger the wall shear stress is and the vortex strength decays quicker in the nozzle. Thus the change in total mass flow rate is smaller for the same inlet vortex strength with larger surface roughness.

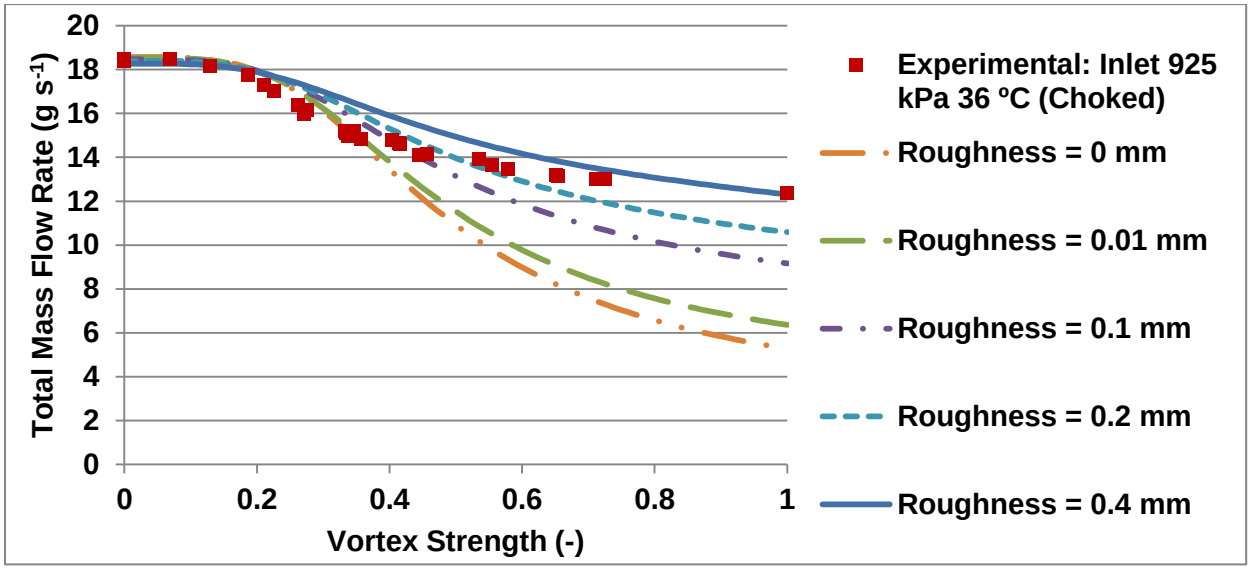

Figure 6: Comparison of choked mass flow rates at different inlet vortex strength from the experiments with modeling results by approach 2 at constant inlet conditions $p_i = 925$ kPa and $T_i = 36$ ℃

The discrepancies between the modeling by the second approach and the experimental results might be due to the following reasons:

- Oversimplification of the flow velocity profile and inappropriate turbulent wall shear stress model.
- Varying metastable pressure in the upstream of the evaporation wave. Vortex strength and depressurization rate may have an influence on the maximum achievable degree of metastability.
- Vortex strength may have significant decay as the vortex flow travels from the vortex nozzle tangential inlet to the starting point of the convergent part of the nozzle.

6. CONCLUSIONS

Two approaches have been employed to model the initially subcooled flashing vortex flow in the nozzle at steady state. The first approach assumes that bubble nucleation during the depressurization in the nozzle all occurs at the nozzle wall. The second approach assumes that there is an evaporation wave at the nozzle throat and the fluid in the upstream of the evaporation wave is assumed to be single-phase incompressible liquid. When the flow is choked, constant degree of metastability in the upstream of the evaporation wave has been assumed for the same nozzle inlet pressure and temperature. The simulation results by the first approach suggest that the bubble nucleation may not all occur at the nozzle wall at high degree of metastability. Nucleation in the bulk of the liquid might be dominant and should possibly be taken into consideration in the modeling. The results achieved by the second approach show better agreement with the experimental results for choked flow. Pressure reduction is required for the kinetic energy increase in the azimuthal direction when there is inlet vortex introduced. Therefore, for the same mass flow rate through the nozzle, the pressure difference from the nozzle inlet to the center of the nozzle throat increases as the inlet vortex becomes stronger. Since the metastable pressure at the throat when the flow is choked is assumed to be constant for the same nozzle inlet pressure and temperature, less mass flow rate can be driven through the nozzle with stronger inlet vortex. The change in total mass flow rate is smaller for the same inlet vortex strength with larger surface roughness. The discrepancies between the modeling with the second approach and experimental results might be due to oversimplification of the flow velocity profile and inappropriate turbulent wall shear stress model, influence of vortex strength and depressurization rate on the maximum achievable degree of metastability, and the decay of vortex strength as the vortex flow travels from the vortex nozzle tangential inlet to the starting point of the convergent part of the nozzle.

NOMENCLATURE

C_D	drag coefficient	(–)
D	diameter	(m)
F	force	(N)
h	heat transfer coefficient	(W m^{-2} K^{-1})
h_{fg}	enthalpy of vaporization	(J kg^{-1})
K	thermal conductivity	(W m^{-1} K^{-1})
m	mass	(kg)
$\dot{m}$	mass flow rate	(kg s^{-1})
Nu	Nusselt number	(–)
p	pressure	(kPa)
Pr	Prandtl number	(–)
r	radial distance	(m)
R	radius	(m)
Re	Reynolds number	(–)
t	time	(s)
T	temperature	(℃)
u	specific internal energy	(J kg^{-1})
v	velocity	(m s^{-1})
V	volume	(m^3)

Greek Symbols

ϵ	surface roughness	(mm)
λ	friction factor	(–)
μ	dynamic viscosity	(Pa s)
Π	degree of metastability	(–)
ϕ	azimuth angle	(rad)
ρ	density	(kg m^{-3})
τ	shear stress	(Pa)
θ	polar angle	(rad)
σ	surface tension	(N m^{-1})

Subscript

c	cavity
depart	departure
i	inlet
meta	metastable
N	nozzle
o	outlet
s	surface
sat	saturation
tan	tangential inlet

REFERENCES

1. Abuaf, N., Jones, O. C., Wu, B. J. C., 1983, Critical flashing flows in nozzles with subcooled inlet conditions, *J. Heat Transf*., vol. 105, no. 2: p. 379-383.
2. Blinkov, V. N., Jones, O. C., Nigmatulin, B. I., 1993, Nucleation and flashing in nozzles-2. Comparison with experiments using a five-equation model for vapor void development, *Int. J. Multiphas. Flow.*, vol. 19, no. 6: p. 965-986.
3. Edwards, A. T., O'Brien, T. P., 1970, Studies of phenomena connected with the depressurization of water reactors, *United Kingdom Atomic Energy Authority*, Risley, Eng..
4. Elbel, S., Hrnjak, P., 2008, Experimental validation of a prototype ejector designed to reduce throttling losses encountered in transcritical R744 system operation, *Int. J. Refrig*., vol. 31, no. 3: p. 411-422.
5. Lawrence, N. and Elbel S., 2014, Experimental investigation of a two-phase ejector cycle suitable for use with low-pressure refrigerants R134a and R1234yf, *Int. J. Refrig*., vol. 38: p. 310-322.
6. Shin, T. S., Jones, O. C., 1993, Nucleation and flashing in nozzles-1. A distributed nucleation model, *Int. J. Multiphas. Flow.*, vol. 19, no. 6: p. 943-964.
7. Simoes-Moreira, J. R., Bullard, C. W., 2003, Pressure drop and flashing mechanisms in refrigerant expansion devices, *Int. J. Refrig.*, vol. 26, no. 7: p. 840-848.
8. Simoes-Moreira, J. R., Shepherd, J. E., 1999, Evaporation waves in superheated dodecane, *J. Fluid Mech*., vol. 382: p. 63-86.
9. Sumeru, K., Nasution, H., Ani, F. N., 2012, A review on two-phase ejector as an expansion device in vapor compression refrigeration cycle, *Renew. Sust. Energ. Rev.*, vol. 16, no. 7: p. 4927-4937.
10. Whitaker, S., 1972, Forced convection heat transfer correlations for flow in pipes, past flat plates, single cylinders, single spheres, and for flow in packed beds and tube bundles, *AIChE J*., vol. 18, no. 2: p. 361-371.
11. Zhu, J. and Elbel, S., 2016, A new control mechanism for two-phase ejector in vapor compression cycles for automotive applications using adjustable motive nozzle inlet swirl, *SAE Int. J. Passeng. Cars - Mech. Syst*., vol. 9, no. 1, doi: 10.4271/2016-01-0243.

ACKNOWLEDGEMENT

The authors would like to thank the member companies of the Air Conditioning and Refrigeration Center at the University of Illinois at Urbana-Champaign for their support.